

# WALL RESOLVED LARGE EDDY SIMULATION OF A FLOW THROUGH A SQUARE-EDGED ORIFICE IN A ROUND PIPE AT RE=25000

**Benhamadouche S. and Arenas M.**

EDF R&D

6, Quai Watier, 78401 Chatou, France

sofiane.benhamadouche@edf.fr; mario.arenas@edf.fr

**Malouf W. J.**

Department of Civil and Environmental Engineering

Imperial College London, London SW7 2AZ, United Kingdom

wadih.malouf10@alumni.imperial.ac.uk<sup>1</sup>

## ABSTRACT

The orifice plate is a pressure differential device frequently used for flow measurements in pipes across different industries. This study demonstrates the accuracy obtainable using a wall-resolved Large Eddy Simulation (LES) implemented in *Code\_Saturne* to predict the velocity, Reynolds stresses, pressure loss and discharge coefficient for a flow through a square-edged orifice in a round pipe at a Reynolds number of 25000. The ratio of the orifice diameter to the pipe diameter is  $\beta = 0.62$ , and the ratio between the orifice thickness to the pipe diameter is 0.11. The mesh is sized using preliminary RANS results to ensure that the solution is resolved beyond the Taylor micro-scale; this is verified *a posteriori*. The inlet condition is simulated using a recycling method, and the LES is run with a dynamic Smagorinsky sub-grid scale (SGS) model. The sensitivity to the SGS model and the pressure-velocity coupling is shown to be negligible. The effect of the inlet condition is also studied, but the impact is also determined to be very small. The LES is compared with the available experimental data and ISO 5167-2. In general, the LES shows good agreement with the velocity from the experimental data. The profiles of the Reynolds stresses are similar, but an offset is observed in the diagonal stresses. The pressure loss and discharge coefficients are shown to be in good agreement with the predictions of ISO 5167-2. Therefore, the wall-resolved LES is shown to be highly accurate in simulating the flow across a square-edged orifice and could be used as reference data for RANS validation.

## KEYWORDS

wall-resolved LES, orifice plate, discharge coefficient

## 1 INTRODUCTION

The orifice flowmeter is a commonly used instrument for flow measurements in pipes. The simple device utilises a known relationship between a pressure drop and a velocity to measure the flowrate across an orifice plate. Given the simplicity and reliability of the tool, it is used across many industries for single phase flow measurements.

The use of the orifice flowmeter is standardised in ISO 5167-1 and ISO 5167-2 [1] [2]. Pressure taps are taken both upstream and downstream of the orifice plate, and the flow velocity can be calculated from equation (1):

---

<sup>1</sup> Current Address: BP ICBT, Sunbury-on-Thames TW16 7LN, wadih.malouf@uk.bp.com

$$u_0 = \frac{C_D}{\sqrt{1-\beta^4}} \epsilon \sqrt{\frac{2\Delta P}{\rho}}, \quad (1)$$

where  $u_0$  is the flow velocity,  $C_D$  is the discharge coefficient,  $\beta$  is the ratio between the orifice and the pipe inner diameters,  $\epsilon$  is the expansibility coefficient,  $\Delta P$  is the pressure drop and  $\rho$  is the fluid density. The discharge coefficient and its uncertainty can be calculated using the Reader-Harris/Gallagher equation [2]. The coefficient is a function of the geometry, the Reynolds number, the placement of the pressure taps and upstream and downstream flow features (such as bends, tees or valves). ISO TR12767 [3] covers some deviations from the scope of ISO 5167-1 and ISO 5167-2.

The minor loss coefficient,  $\xi$  is defined as the ratio between pressure loss across the orifice plate and the velocity head  $\rho u_0^2/2$ . It can be estimated in accordance with ISO 5167-2 from equation (2):

$$\xi_{ISO} = \left( \frac{\sqrt{1-\beta^4(1-C_{D,ISO}^2)}}{C_{D,ISO}\beta^2} - 1 \right)^2 \quad (2)$$

As a result of the widespread use of orifice plates and a need to use them beyond the scope of ISO 5167-1 and ISO 5167-2, there is an interest in numerical simulations to better understand different aspects of the flow. This includes numerical predictions of the discharge coefficient, mass and thermal transfer mechanisms and pressure losses across the device.

The literature shows that wall-modelled Reynolds Averaged Navier-Stokes (RANS) simulations can reasonably predict the discharge coefficient, albeit with a high dependency on discretisation errors and on the turbulence model. Erdal and Andersson [4] show in a two-dimensional axisymmetric simulation of an orifice plate with a standard and modified  $k-\epsilon$  model that the pressure drop across the orifice plate is highly dependent on the grid refinement around the orifice plate and the turbulence model used. Shah et al. [5] model the orifice flowmeter with a standard  $k-\epsilon$  model to show that the pressure recovery downstream of the orifice plate is not well predicted. More recently, Shaaban [6] shows that the realizable  $k-\epsilon$  turbulence is within 1.4% of the ISO estimate of the discharge coefficient. Benhamadouche et al. [7] show that the RSM SSG [8] and  $k-\omega$  SST [9] turbulence models with near wall modelling provide reasonable estimates of the discharge coefficient on a circular square-edged orifice at Reynolds 25000, while the results of the standard  $k-\epsilon$  and  $k-\epsilon$  with linear production [10] turbulence models are not accurate. However, they show that all models with near wall modelling have a high dependency on the spatial discretisation. Benhamadouche et al. [7] also study a RANS simulation with near wall resolution using the EB-RSM [11] turbulence model. The EB-RSM simulation reasonably predicts the discharge coefficient, and it shows a significantly reduced dependency on the spatial discretisation [7].

Although RANS simulations could reasonably predict the discharge coefficient in certain simulations, first and second order statistics downstream of the orifice plate diverge significantly from experimental data. Erdal and Andersson [4] demonstrate that the standard  $k-\epsilon$  turbulence model does not accurately capture the physics of the flow especially around the region at which the fluid accelerates across the pipe. Benhamadouche et al. [7] establish that the maximum centreline velocities downstream of the orifice plate are under-predicted by the  $k-\epsilon$  and  $k-\epsilon$  with Linear Production. They also shown that the EB-RSM, RSM SSG and  $k-\omega$  SST turbulence models reasonably predict the maximum centreline velocities; however, they all fail to qualitatively predict the centreline velocities  $x/R \geq 2$  downstream of the orifice plate.

A review of the literature has not found a simulation technique that can reasonably predict both the pressure drop and first and second order statistics downstream of the plate. Therefore, it is of interest to study the precision obtainable with a wall-resolved Large Eddy Simulation (LES) and compare the results to detailed experimental data.

## 2 TEST CASE

The LES is based on the test case of Shan et al. who use a planar particle image velocimetry (PIV) to measure the flow field downstream of a circular square-edged orifice plate in a round pipe [12]. This test case is also used in Benhamadouche et al. for RANS simulations [7]. The computational domain of the test case is shown in Figure 1. The relevant parameters are:

- $\rho = 996.65 \text{ kg/m}^3$ ;
- $\mu = 8.54 \times 10^{-4} \text{ Pa.s}$ ;
- $D = 46 \text{ mm}$ ;
- $\beta = 0.62$ ;
- $t = 5 \text{ mm}$ ;

where  $\rho$  is the fluid density,  $\mu$  the dynamic viscosity,  $D$  the pipe inner diameter,  $d$  the orifice diameter,  $\beta$  the ratio between the orifice and the pipe inner diameters, and  $t$  the thickness of the orifice plate.

The pipe wall is assumed to be smooth, and the bulk Reynolds number measured using the flow velocity and pipe diameter is  $Re_{bulk} = 25000$ .

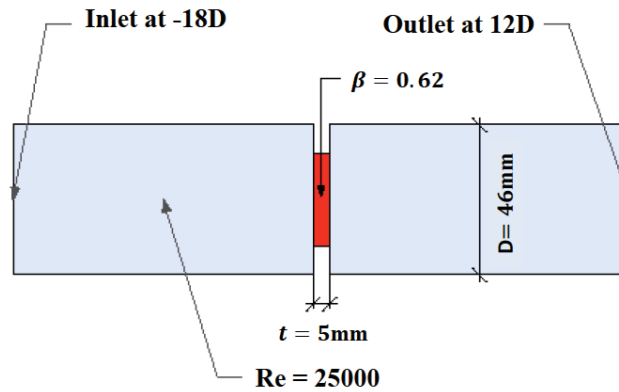


Figure 1: Computational domain and boundary conditions

The mean velocity fields and turbulent fields from the stereoscopic PIV are given in [12].

The ISO 5167-2 estimates are calculated in [7]. The discharge coefficient,  $C_{D,ISO} = 0.628 \pm 0.005$  and the minor loss coefficient  $\xi_{iso} = 8.71 \pm 0.07$ .

## 3 NUMERICAL APPROACH

### 3.1 Large Eddy Simulations with *Code\_Saturne*

*Code\_Saturne* is a highly customisable open source ([www.code-saturne.org](http://www.code-saturne.org)) CFD package developed by EDF. It is based on a co-located finite volume discretisation and accepts unstructured mesh types. Velocity and pressure coupling is ensured *via* the SIMPLEC algorithm. The pressure Poisson equation is solved using an algebraic multigrid. Further information can be found in [13]. The LES capabilities of *Code\_Saturne* have been validated on various academic and industrial cases including decaying isotropic turbulence, side-by-side cylinders and gusts over a plate; see [14], [15] and [16] for example.

The temporal discretisation for the LES is second order Crank-Nicolson in time with linearised convection. The spatial discretisation is a pure second order central difference scheme.

The sub-grid scale models used are the Dynamic Smagorinsky [17], [18], [20] as a base case and the standard Smagorinsky [19] and no SGS model to test sensitivities. Further details about the implementation of LES in *Code\_Saturne* can be found in [14]. In the dynamic model, negative values of the Smagorinsky constant are not allowed and its maximum value is set de 0.065. In the standard Smagorinsky model, the constant is set to  $C_s = 0.065$  and a Van Driest damping function is used.

The inlet is located  $18D$  upstream, and the outlet is located  $12D$  downstream. The distance of the inlet and outlet from the area of interest is based on previous studies with *Code\_Saturne* with similar

geometries. The inlet profile is simulated through a recycling method. At the first time step, artificial eddies are created using the synthetic eddy method [20]. However, the flow 6D downstream of the inlet is then reused as the input to simulate a pseudo-periodic precursor method, creating a fully developed turbulent flow [21]. The standard outlet condition of *Code\_Saturne* is applied. The pressure at the cell face at time step “ $n + 1$ ” is equal to the pressure at the corresponding cell centre at time step “ $n$ ”, and the normal derivative of the velocity vector is zero.

The time step is constant, and it is initially chosen to ensure a CFL less than 1 throughout solution domain. However, it is later increased such that there are highly localised CFL values greater than one. As the time scheme is second-order implicit, these highly localised CFL values greater than one are deemed acceptable since they do not cause any observed numerical instabilities.

### 3.2 Mesh Generation

A mesh is prepared for the LES using *ICEM CFD v14.0*. The mesh is structured in the streamwise direction, and it is locally refined in the streamwise direction near the orifice. It also must be noted that the mesh is perfectly aligned in the streamwise direction. This is important for the recycling method to generate the fully developed turbulent flow. Moreover, the mesh is conformal throughout the domain. This is also important, as non-conformal interfaces are known to be unsuitable in LES since they may introduce significant numerical errors. The cell size is determined using RANS results from [7] to ensure that the solution is resolved beyond the Taylor micro-scale, which is taken equal to  $\sqrt{15\nu k/\epsilon}$ , where  $k$  is the turbulent kinetic energy,  $\nu$  the kinematic viscosity and  $\epsilon$  the turbulent dissipation rate. The upstream wall shear velocity is approximately  $u_* = 0.025 \text{ m/s}$ . This roughly gives a maximum non-dimensional azimuthal length of 12, a maximum non-dimensional radial length of 10, and a maximum non-dimensional streamwise length of 40 (the values are based on the friction velocity upstream of the orifice). The mesh consists of approximately 55 million cells.

The resolution beyond the Taylor micro-scale is also verified *a posteriori* using spectral analysis of time values at key locations. This is shown later in Section 6.3.

The non-dimensional wall distance  $y^+$  is kept below 1 across almost whole domain, ensuring an accurate wall resolved LES; the refinement in the two other directions being also below the requirements for a well resolved LES. This is shown in Figure 2. Locally, in the reattachment zone,  $y^+ \approx 1.5$  can be observed; however, these impact points are highly local, and they only span a short period of time.

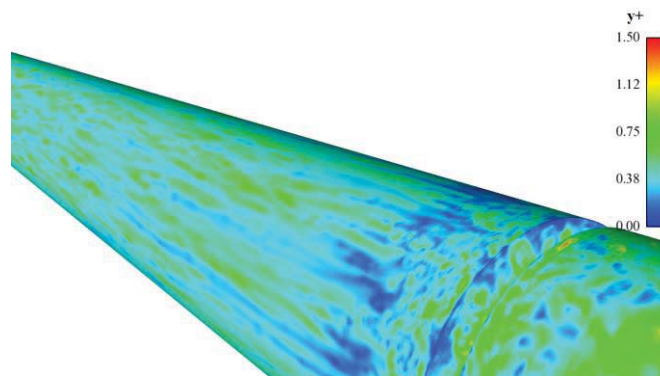


Figure 2: Non-dimensional wall distance  $y^+$  of the first cell centre

## 4 STATISTICS

The simulations were performed with the Blue Gene/Q supercomputer, using a total of 256 nodes (4,096 processors - Power BQC 16C 1.6GHz) over 6 day queues. Each time step was  $1 \times 10^{-5} \text{ s}$  which typically took around 1s to solve.

#### 4.1 Temporal Statistics

After approximately 5 flow-passes in the recycled pipe, the inlet profile is deemed to be developed, and the turbulent flow structures have passed through the solution domain. The instantaneous azimuthal velocity field at the inlet is shown in Figure 3; the structures are characteristic of a fully developed turbulent flow in a pipe. An instantaneous stream-wise velocity field near the orifice is also given in Figure 4. The non-dimensional wall distance  $y^+$  of the first cell shown in Figure 2 exhibits the characteristic low speed streaks expected between  $0 < y^+ < 10$  [22].

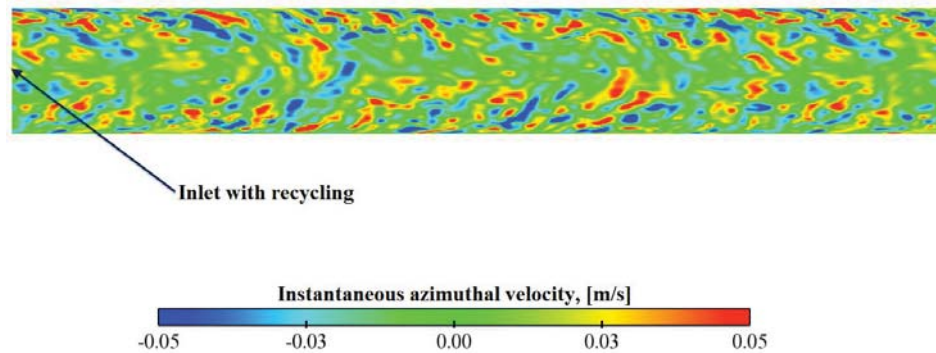


**Figure 3: Azimuthal (out of plane) instantaneous velocity profile near the inlet at around after approximately 5 flow-passes across the recycled pipe**

From this point, the velocity, pressure and Reynolds stresses are averaged in time. The flow is averaged until approximately 7 flow-passes across the domain corresponding to  $2.2 \times 10^6$  iterations for the dynamic Smagorinsky model and 4.5 flow-passes across the domain corresponding to  $1.3 \times 10^6$  iterations for the other sub-grid scale models.

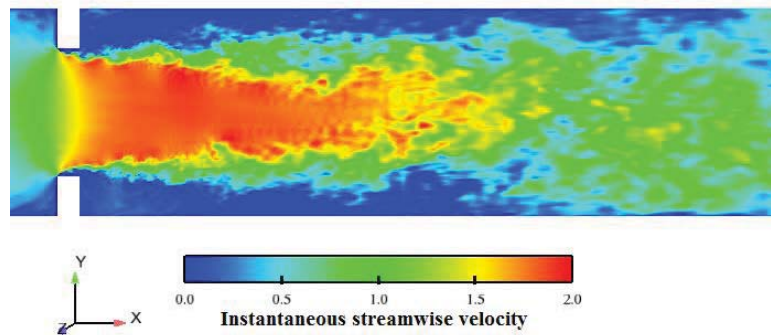


**Figure 4: Instantaneous streamwise velocity after approximately 1 flow-pass across the entire domain**

#### 4.2 Axisymmetry of Temporal Averages

It is assumed *a priori* that the temporal averages of all quantities are axisymmetric in the round pipe both upstream and downstream of the orifice plate. This assumption is verified *a posteriori*; Figure 5 shows turbulent kinetic energy and wall pressure coefficient profiles averaged in the azimuthal direction compared to local ones (not averaged in the azimuthal direction) after 6 flow-passes. The difference between the local profile and averaged profile is very small, and this is true for first and second order statistics. This argument is used to reduce the total number of calculations for the simulations studying the sensitivity of the model, as the flow is only averaged for 4 flow-passes across the domain and then averaged about the azimuth.



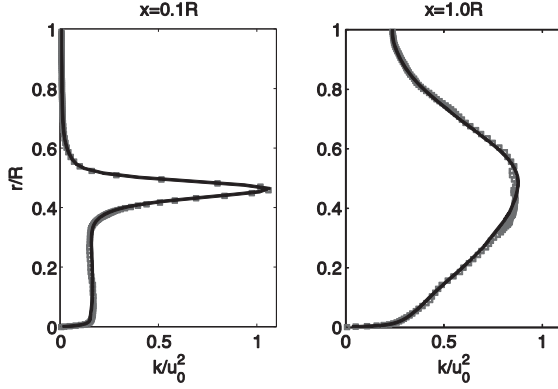


Figure 5a: Turbulent kinetic energy  $k$

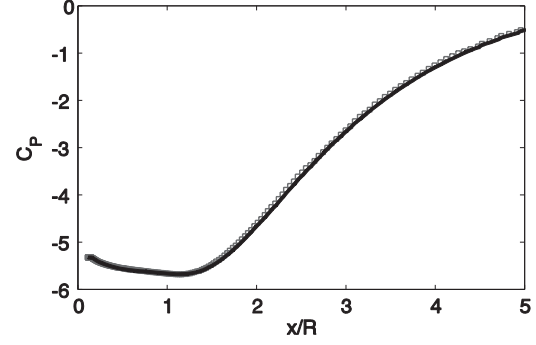


Figure 5b: Wall pressure coefficient  $C_p$

Figure 5: Comparison between azimuthally and non-azimuthally averaged data.  
□, non-azimuthal average, —, azimuthal average<sup>2</sup>.

## 5 SENSITIVITY STUDIES

Sensitivity studies of the LES are performed evaluating the sub-grid scale model. Although this approach does not explicitly address the numerical error, it investigates the modelling error and indirectly assesses the numerical error. Moreover, the number of external sweeps on the pressure-velocity coupling is examined. The sensitivity study is performed using time-averaged values.

### 5.1 Sub-Grid Scale Model

The most advanced sub-grid scale model used in the present study is the dynamic Smagorinsky one. Nonetheless, the standard Smagorinsky model and a simulation without a sub-grid scale model are compared. The three approaches are outlined in Section 3.1.

The profiles show no significant differences between the three different SGS models, as seen in Figure 6. The very small difference between the three sub-grid scale models indicates that the modelling error is sufficiently small.

In addition to the profiles, the reattachment points in the recirculation zone and pressure loss coefficient for the three models are given in Table 1. The pressure loss calculation is outlined in Section 1. The downstream recirculation reattachment points are determined as the point at which the wall shear stress,  $\tau_{wall}$  changes direction, and are given in non-dimensional distances from the downstream face of the orifice plate.

The overall pressure loss is not very sensitive to the SGS model. The primary reattachment length is more dependent on the sub-grid scales model than the discharge or pressure loss coefficients. The most significant difference arises between the dynamic Smagorinsky model and the constant Smagorinsky model, while the LES without an SGS model is reasonably similar to the dynamic Smagorinsky model.

The better agreement between the dynamic Smagorinsky and LES with no SGS model is hypothesised to be a result of  $C_s$  tending to zero as the filter width decreases relative to the Kolmogorov scale, as shown with a Lilly type analysis [23] [24].

However, the close resemblance between all three models demonstrates that the LES is well resolved beyond the Taylor micro-scale, as the influence of the SGS model is almost negligible.

<sup>2</sup> The pipe centreline is at  $r/R = 1$ . All distances in the stream-wise direction are downstream of the centre of the orifice plate.

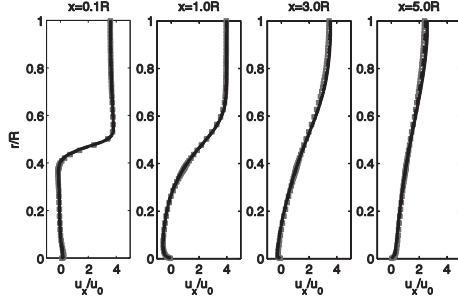


Figure 6a: Streamwise velocity,  $u_x$

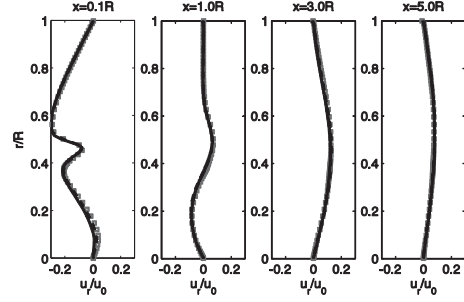


Figure 6b: Radial velocity,  $u_r$

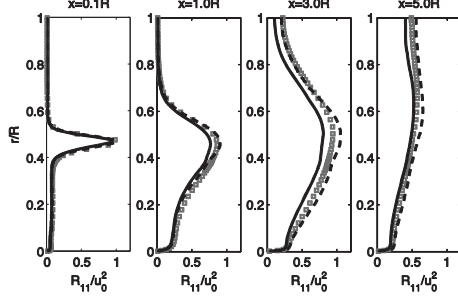


Figure 6c:  $R_{11} = \overline{u'_x u'_x}$

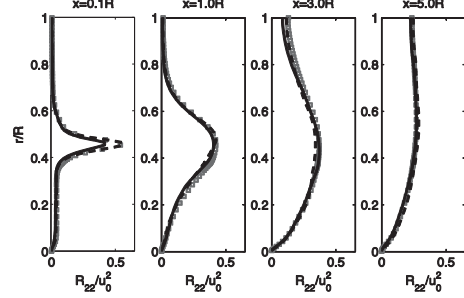


Figure 6d:  $R_{22} = \overline{u'_r u'_r}$

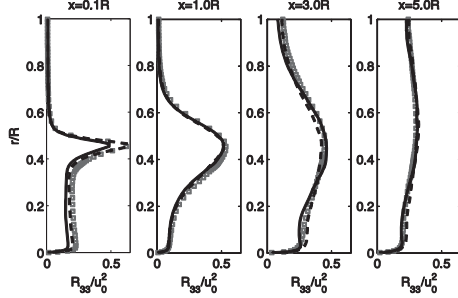


Figure 6e:  $R_{33} = \overline{u'_\theta u'_\theta}$

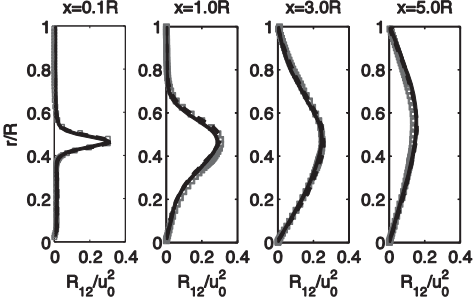


Figure 6f:  $R_{12} = \overline{u'_x u'_r}$

Figure 6: Comparison between different SGS model.  $\square$ , dynamic Smagorinsky,  $-$ , Smagorinsky,  $- -$ , no SGS.

Table 1: Recirculation lengths and pressure loss for the three LES simulations

	Dynamic Smagorinsky	Constant Smagorinsky	No Sub-grid Scale Model
Pressure loss coefficient	8.64	8.79	8.71
Primary reattachment $[x/R]$	3.92	4.25	4.11
Secondary reattachment $[x/R]$	0.42	0.37	0.40
Tertiary reattachment $[x/R]$	0.025	0.020	0.023

## 5.2 Inlet Boundary Condition

The distance at which the flow is recycled is verified by observing the dominant frequencies downstream of the orifice. The representative frequency at which the flow is recycled is  $F = \frac{u_0}{6D} \approx 1.7\text{Hz}$ . 18 probes

are placed across the domain, of which 6 are downstream of the orifice. The spectrum of the velocity field is calculated for all the points downstream of the orifice, an example of which is found in Figure 7<sup>3</sup>.

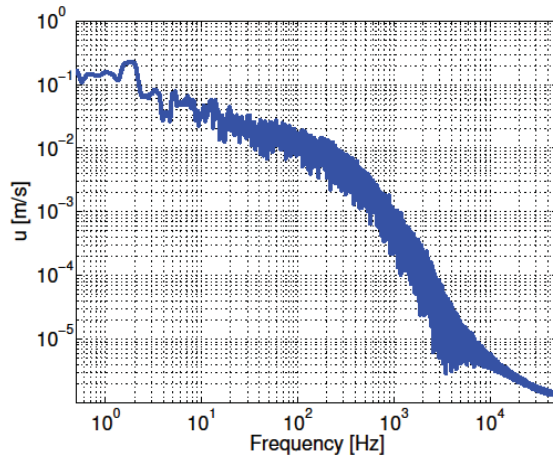


Figure 7a: Full spectrum

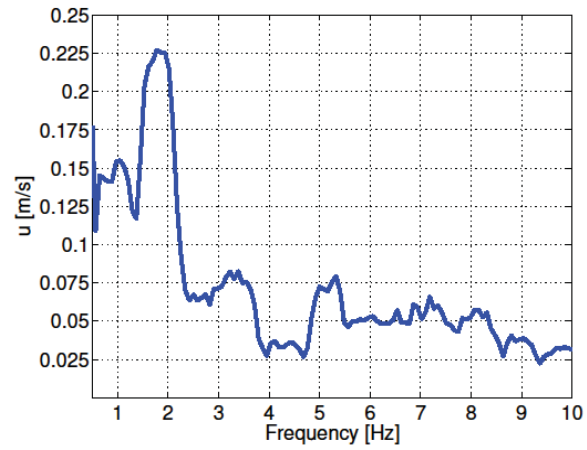


Figure 7b: Spectrum around 2Hz

Figure 7: Streamwise velocity spectrum 1D downstream of the orifice at the step height.

A small peak is observed, corresponding to roughly 2Hz. Note that Figure 7 corresponds to the largest peak observed around 2Hz out of all the probes upstream and downstream of the orifice plate. It is postulated that this peak comes from the recycling method used at the inlet. Nonetheless, the magnitude of this peak is relatively small and its appearance is highly localised (as shown by the spectra in Section 6.3).

### 5.3 Pressure-Velocity Coupling

The number of sweeps (outer iterations) of the pressure-velocity coupling is increased for the Dynamic Smagorinsky model. The standard cases only iterate once about the SIMPLEC pressure velocity coupling. In this test, the number of sweeps is increased to three, and it is averaged for approximately 3 flow-passes across the domain.

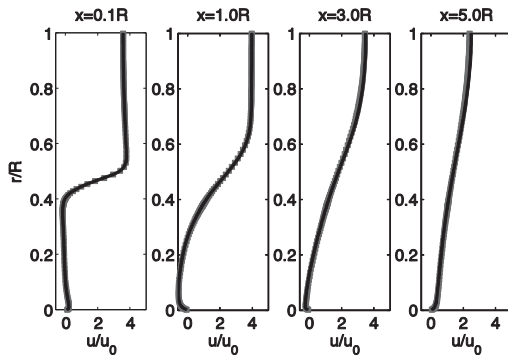


Figure 8a: Streamwise velocity,  $u_x$

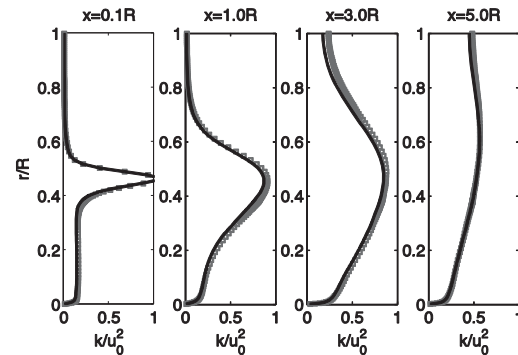


Figure 8b: Turbulent kinetic energy,  $k$

Figure 8: Comparison between sweeps on the pressure-velocity coupling.  $\square$ , single sweep,  $-$ , three sweeps.

<sup>3</sup> The spectra in this section are estimated using a Thomson multitaper method [25].



It is found that the differences between the two simulations are very small. For example, the difference between the predicted pressure loss coefficient is approximately 0.5%, and the velocity and turbulent kinetic energy profiles do not change, as seen in Figure 8. It can thus be concluded that one sweep about the pressure-velocity coupling is sufficient.

## 6 COMPARISONS WITH EXPERIMENTAL DATA

LES with the dynamic Smagorinsky model is compared with PIV data from [12]. The average inflow velocity  $u_0$  from the experimental data is used to normalise the PIV data. It is noted that the centreline stream-wise velocity normalised by the average velocity shows very similar behaviour between the PIV observations and LES, as seen in Figure 9.

Moreover, the shapes of both the LES and PIV stream-wise and radial velocity profiles provide a close match, as seen in Figure 10a and Figure 10b. The results differ in two important zones. The first is in the regions of high gradients of the velocity. The second is in the near wall region. This is not surprising for the latter, as the PIV methodology is known to lose accuracy in the near wall region. With regards to the results in the regions of high gradients, the resolution of the PIV is larger than the grid size of the LES; thus smoothing the results. For example, near  $r/R = 0.6$ , as seen in Figure 10b, the LES predicts a much larger variation than the PIV for the radial velocity. At this point, the LES radial mesh length is 0.0018D, while the PIV pixel size is 0.014D, almost 8 times larger.

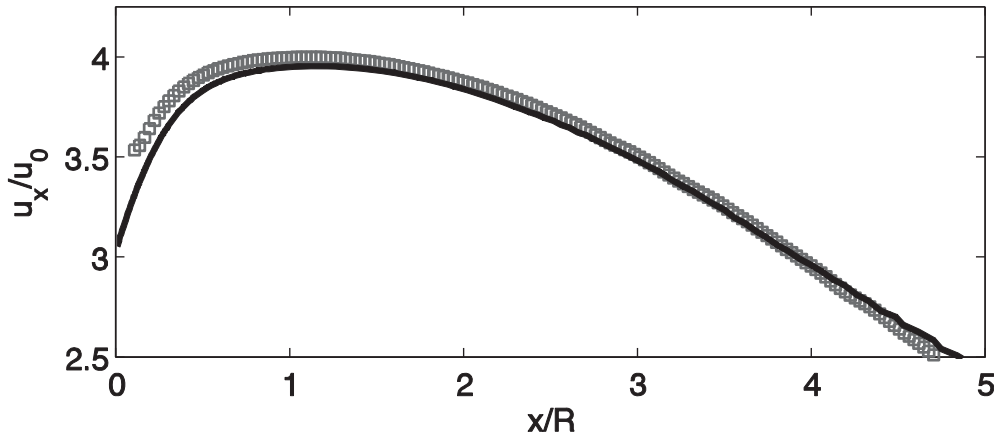


Figure 9: Stream-wise centreline velocity profile downstream of the orifice. □, experimental data, —, LES.

Lastly, the normalised mean Reynolds stresses  $R_{11}$  and  $R_{12}$  corresponding to  $\overline{u'_x u'_x}$  and  $\overline{u'_x u'_r}$ , respectively, can be compared. Note that  $R_{22}$  results are very similar to the results of  $R_{11}$ , and is therefore not shown. It is noticed that the experimental and LES profiles of  $R_{12}$  are reasonably similar with the exception of areas with large gradients as shown in Figure 10. On the other hand, the normalised profile of  $R_{11}$  shows large differences even outside regions with large gradients.

The difference between the experimental and simulated  $R_{11}$  profiles is almost constant, and it is likely to arise from three possible sources. The first is that the numerical simulation under-predicts the mean Reynolds stresses in the flow. This is least likely since the numerical mean velocity is well predicted which is not possible if the Reynolds mean stresses are severely under-predicted. This hypothesis is also not likely since the  $R_{12}$  profile does not exhibit the same offset as the profiles of  $R_{11}$  and  $R_{22}$ . The second possibility arises from an insufficient time average for either the numerical or experimental data. With regards to the numerical data, a time series approximately 50% shorter for the dynamic Smagorinsky model (3 flow-passes across the domain of averaging) shows no significant difference in the profiles of  $R_{12}$ . Moreover, this doesn't explain the differences between  $R_{11}$  or  $R_{22}$  while the profiles of  $R_{12}$  are similar.

The last possibility arises in the method of which the experimental diagonal stresses are calculated. It is assumed that  $R_{ii} = u_{i,\text{rms}}^2$  which corresponds to the assumption that  $\text{Var}[u_i] = R_{ii}$ . This hypothesis fails to take into account that the act of measuring the flow introduces a precision error. As a result, the experimental  $\text{Var}[u_i] = R_{ii} + \text{Error}_i$ , where  $\text{Error}_i$  is the precision error as a result of measurement in the  $i^{\text{th}}$  direction and  $R_{ii}$  is a result of the physical turbulent fluctuations. Assuming that the measurement errors in the  $i^{\text{th}}$  and  $j^{\text{th}}$  are independent, the covariance between  $u_i$  and  $u_j$  is also independent of a measurement error; therefore,  $\text{Cov}(u_i, u_j) = R_{ij}$ . For this reason, it is possible that the large and constant difference between the experimental and numerical  $R_{ii}$  can largely be attributed to the measurement error. This does not discount other sources of error in both the LES and PIV, but it provides an explanation for the source of a constant difference only in the profiles of  $R_{11}$  and  $R_{22}$  only.

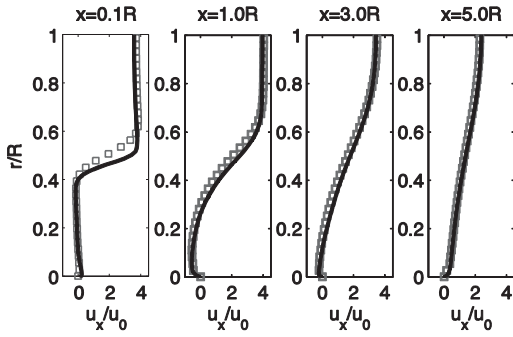


Figure 10a: Normalised stream-wise velocity

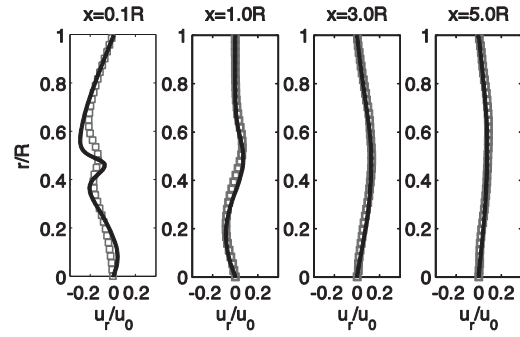


Figure 10b: Normalised radial velocity

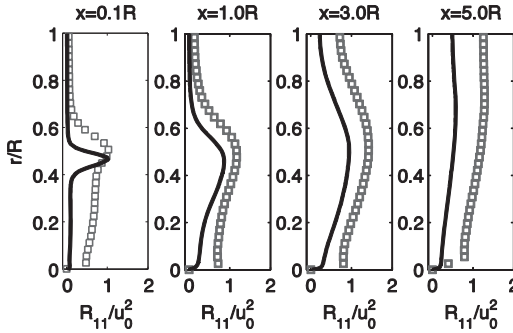


Figure 10c: Normalised  $R_{11}$

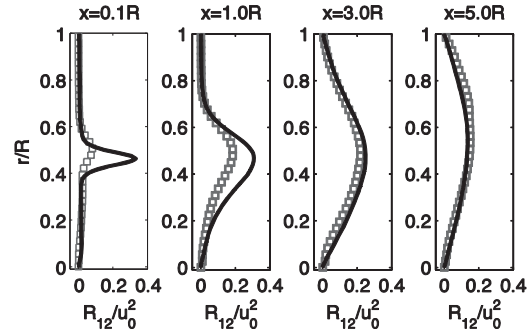


Figure 10d: Normalised  $R_{12}$

Figure 10: Comparison between LES and PIV profiles.  $\square$ , experimental data,  $—$ , LES.

## 6.1 Recirculation Zones

The PIV predicts a reattachment length of the primary recirculation zone  $x = 3.64R$  downstream of the orifice using the forward flow probability (FFP) method [12]. From the LES, the reattachment length is estimated at  $x = 3.92R$  downstream of the orifice. However, the difference between the data is due to the method in which the reattachment length is calculated. The LES estimate determines the reattachment length as the point at which the wall shear stress changes direction. Since the near wall region is resolved, the velocity distribution is linear in the radial direction (normal to the wall); therefore  $\tau_{\text{wall}} = \mu \frac{u^{(1)}}{r^{(1)}}$  where  $u^{(1)}$  is the velocity at the centre of the first cell from the wall, and  $r^{(1)}$  is the distance of that cell centre to the wall. This is analogous to the mean stream-wise velocity zero-crossing estimate, where the reattachment zone is the point at which the velocity changes sign.

The PIV estimate of the reattachment point uses a FFP at  $y = 0.056R$  away from the wall which corresponds to twice the resolution of the technique adopted [12]. The FFP method calculates a probability density function of the stream-wise velocity being positive. The reattachment length is then given by the point at which the probability of the velocity being positive is exactly 50%. Using the experimental data, it is possible to estimate the recirculation zone using a mean stream-wise velocity zero-crossing method. The first point located  $y = 0.028R$  away from the wall is used to estimate the velocity. This method predicts a primary reattachment length  $x = 3.62R$  downstream of the orifice, and the secondary reattachment length is found at  $x = 0.27R$ . A similar approach for the LES results in a primary reattachment length of  $x = 3.60R$  and a secondary reattachment length of  $x = 0.34R$ . Therefore, it is clear that the predicted reattachment points calculated with the same methodology using PIV data and the LES are similar.

## 6.2 Pressure Loss Coefficient and Discharge Coefficient

The discharge coefficient of the dynamic Smagorinsky LES is calculated by taking pressure taps  $1D$  upstream of the orifice and  $0.5D$  downstream (both measured from the upstream face as required by [2]), resulting in discharge coefficient of  $C_D = 0.632$ . From [7], the ISO 5167-2 estimate for the discharge coefficient is  $0.628 \pm 0.005$ .

The pressure loss across the orifice is measured between  $2D$  upstream and  $6D$  downstream, where the stream-wise variation in the wall pressure is deemed to be linear. Using the dynamic Smagorinsky model, the minor loss coefficient is  $\xi = 8.64$ . Similarly, the estimate from ISO 5167-2 is  $8.71 \pm 0.07$  [7].

The results between the ISO standards and the LES are in very close agreement - within the margin of error of the ISO estimate - which serves as further validation of the LES results.

## 6.3 Spectral Analysis

A spectral analysis of the simulation is performed to establish whether the filtering operation is taking place in the inertial sub-range, and to establish dominant frequencies in the flow. Note that the centre of the orifice is taken as the point  $x = 0$ .

It is seen in Figure 11 that a large part of the inertial zone is resolved throughout the whole domain. The cascade of energy to the smaller time scales is evident throughout. Moreover, representative points, such as at the step height which lies near the free shear layer, or near the wall, show that this phenomenon is observed in a wide variety of different regimes across the domain. This is further validation that the mesh is sufficiently refined for an LES.

Interesting features can be observed from the velocity spectra. Downstream of the orifice, the spectrum spreads over a significantly larger frequency range. It is also significant that no dominant frequency is observed in none of the calculated velocity spectra. A longer time series must be analysed to confirm the observation regarding dominant frequencies.

Lastly, the velocity spectra of the different velocity components are calculated at the given points. Representative spectra are shown in Figure 12. The anisotropy of the velocity fluctuations is evident at certain points. This is especially prominent near the wall, but it is also observed at the centre of the orifice plate.

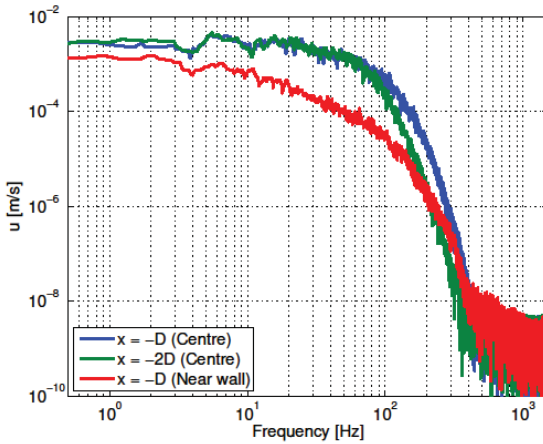


Figure 11a: Upstream of the orifice

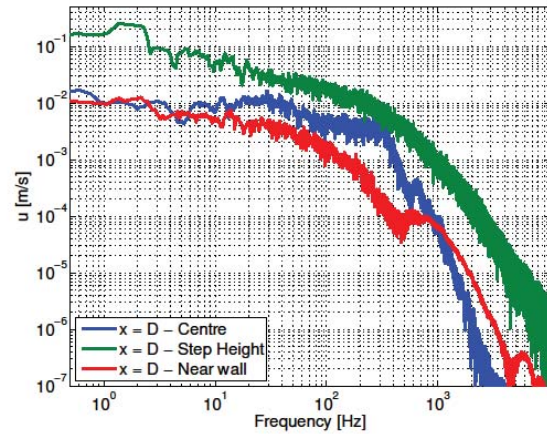


Figure 11b: Downstream of the orifice

Figure 11: Streamwise velocity spectra of representative points.

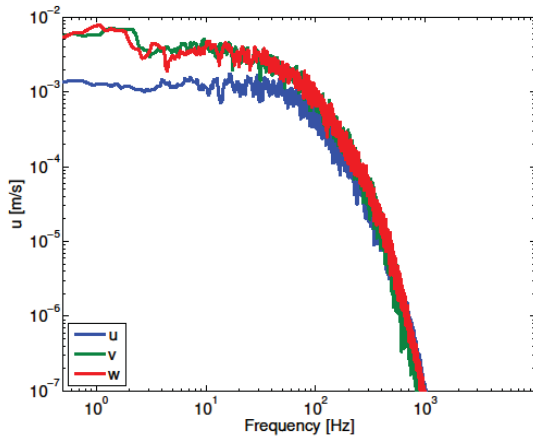


Figure 12a: Centre of the orifice ( $x = y = z = 0$ )

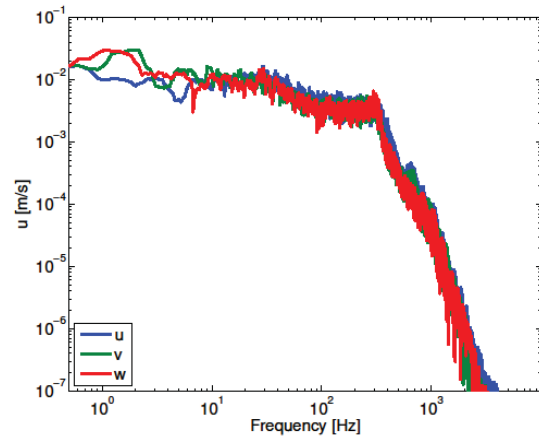


Figure 12b: Centre of the pipe, 1D downstream of the orifice ( $x = D, y = z = 0$ )

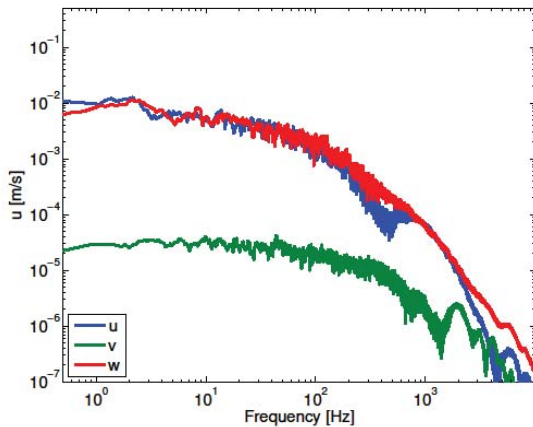


Figure 12c: Near the wall, 1D downstream of the orifice ( $x = D, y = 0.4996D, z = 0$ )

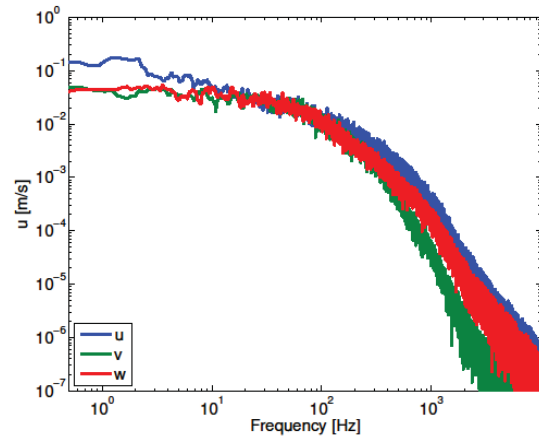


Figure 12d: Step height, 2D downstream of the orifice ( $x = 2D, y = 0.31D, z = 0$ )

Figure 12: Spectra of velocity components at representative points

## 7 CONCLUSIONS

This study demonstrates that a very fine wall-resolved LES with a dynamic Smagorinsky SGS can accurately and precisely simulate a single phase flow through a square-edged orifice flowmeter. A sensitivity study shows that the effect of the SGS model and pressure-velocity coupling is negligible. An analysis of the velocity spectra in critical locations shows a small peak corresponding to the recycling frequency, but the magnitude is very small.

The LES shows excellent agreement with the velocity from the experimental data. There is also good agreement observed between the respective  $R_{12}$  profiles. However, the  $R_{11}$  and  $R_{22}$  profiles show an offset, which could be a result from an error introduced through measurement rather than the LES. Moreover, the recirculation lengths are well predicted by the LES. Lastly, the pressure loss coefficient and discharge coefficient are also shown to be in agreement with the predictions of ISO 5167-2.

Therefore, the wall-resolved LES is shown to be accurate in simulating the flow across a square-edged orifice. The results from this simulation can be used to validate other simulation techniques such as RANS approaches. Moreover, this study shows that the LES is a viable technique in predicting recirculation lengths, discharge coefficient, pressure loss coefficient and mean velocities in an orifice flowmeter. This has important repercussions for the assessment of heat and mass transfer characteristics of industrial orifice flowmeters. This result also shows that the discharge coefficients and pressure loss coefficients should be predictable using the LES technique in non-standard configurations.

## 8 ACKNOWLEDGMENTS

The authors would like to acknowledge Dr. Feng Shan for kindly sharing the experimental results for the test case.

## 9 REFERENCES

1. ISO 5167-1: 2003. Measurement of fluid flow by means of pressure differential devices inserted in circular cross-section conduits running full -- Part 1.
2. ISO 5167-2: 2003. Measurement of fluid flow by means of pressure differential devices inserted in circular cross-section conduits running full -- Part 2.
3. ISO TR 12767: 1998. Measurement of Fluid Flow by Means of Pressure Differential Devices—Guidelines to the Effect of Departure from the Specifications and Operating Conditions given in ISO, 5167.
4. A. Erdal and H. I. Andersson, "Numerical aspects of flow computation through orifices," *Flow Measurement and Instrumentation*, **8**(1), pp. 27-37 (1997).
5. M. S. Shah, J. B. Joshi, A. S. Kalsi, C. S. R Prasad and D. S. Shukla, "Analysis of flow through an orifice meter: CFD simulation," *Chemical Engineering Science*, **71**, pp. 300-309 (2012).
6. S. Shaaban, "Optimization of orifice meter's energy consumption," *Chemical Engineering Research and Design*, **92**(6), pp. 1005-1015 (2014).
7. S. Benhamadouche, W. J. Malouf and M. Arenas, "Effects of spatial discretisation and RANS turbulence modelling on the numerical simulation of a flow through a square-edged orifice in a round pipe", *Proceedings of the 36<sup>th</sup> IAHR World Congress* (accepted), Delft, the Netherlands (2015).
8. C. G. Speziale, S. Sarkar and T.B. Gatski, "Modelling the pressure-strain correlation of turbulence: an invariant dynamical systems approach," *Journal of Fluid Mechanics*, **227**, pp. 245-272 (1991).
9. F. R. Menter, "Two-Equation Eddy-Viscosity Turbulence Models for Engineering Applications," *AIAA Journal*, **32**(8), pp. 1598-1605 (1994).



10. V. Guimet and D. Laurence, "A linearised turbulent production in the  $k-\epsilon$  model for engineering applications," *Proceedings of the 5<sup>th</sup> International Symposium on Engineering Turbulence Modelling and Measurements*, Mallorca, Spain (2002).
11. R. Manceau and K. Hanjalić, "Elliptic blending model: A new near-wall Reynolds-stress turbulence closure," *Physics of Fluids*, **14**(2), pp. 744-754 (2002).
12. F. Shan, A. Fujishiro, T. Tsuneyoshi and Y. Tsuji, "Particle image velocimetry measurements of flow field behind a circular square-edged orifice in a round pipe," *Experiments in Fluids*, **54**(6), pp. 1-18 (2013).
13. F. Archambeau, N. Mechtoua, and M. Sakiz, "Code\_Saturne: A finite volume method for the computation of turbulent incompressible flows: Industrial applications," *International Journal on Finite Volumes*, **1**(1) (2004).
14. S. Benhamadouche, "Large-Eddy Simulation with the unstructured collocated arrangement", PhD thesis, The University of Manchester (2006).
15. I. Afgan, Y. Kahil, S. Benhamadouche and P. Sagaut, "Large eddy simulation of the flow around single and two side-by-side cylinders at subcritical Reynolds numbers," *Physics of Fluids*, **23**(7), 075101 (2011).
16. I. Afgan, S. Benhamadouche, X. Han, P. Sagaut and D. Laurence, "Flow over a flat plate with uniform inlet and incident coherent gusts," *Journal of Fluid Mechanics*, **720**, pp. 457-485 (2013).
17. M. Germano, U. Piomelli, P. Moin, and W. Cabot, "A dynamic subgrid-scale eddy viscosity model," *Physics of Fluids*, **3**(7), pp. 1760-1765 (1991).
18. D. Lilly, "A proposed modification of the Germano subgrid-scale closure method," *Physics of Fluids*, **4**(3), pp. 633-635 (1992).
19. J. Smagorinsky, "General circulation experiments with the primitive equations. I. The basic equations," *Monthly Weather Review*, **91**(3), pp. 99-164 (1963)
20. N. Jarrin, S. Benhamadouche, D. Laurence and R. Prosser. "A synthetic-eddy-method for generating inflow conditions for large-eddy simulations," *International Journal of Heat and Fluid Flow*, **27**(4), pp. 585-593 (2006).
21. E. Lamballais, "Direct numerical simulation of a turbulent flow in a rotating channel with a sudden expansion," *Journal of Fluid Mech.*, **745**, pp. 92-131 (2014).
22. S. B. Pope, *Turbulent flows*, Cambridge university press (2000).
23. P. R. Voke, "Subgrid-scale modelling at low mesh Reynolds number," *Theoretical and computational fluid dynamics*, **8**(2), pp. 131-143 (1996).
24. C. Meneveau and T. S. Lund, "The dynamic Smagorinsky model and scale dependent coefficients in the viscous range of turbulence," *Physics of Fluids*, **9**(12), pp. 3932-3934 (1997).
25. D. J. Thomson, "Spectrum estimation and harmonic analysis," *Proceedings of the IEEE*, **70**(9), pp. 1055-1096 (1982).